
Surrogate Modeling of 3D Rayleigh-Bénard Convection with Equivariant Autoencoders

Fynn Fromme

Lamarr Institute for Machine Learning and Artificial Intelligence (TU Dortmund)
and Karlsruhe Institute of Technology
fynn.fromme@tu-dortmund.de

Christine Allen-Blanchette

Department of Mechanical and Aerospace Engineering
Center for Statistics and Machine Learning
Princeton University
ca15@princeton.edu

Hans Harder

Lamarr Institute for Machine Learning and Artificial Intelligence (TU Dortmund)
and Department of Computer Science at Paderborn University
hans.harder@uni-paderborn.de

Sebastian Peitz

Department of Computer Science and
Lamarr Institute for Machine Learning and Artificial Intelligence
TU Dortmund University
sebastian.peitz@tu-dortmund.de

Abstract

The use of machine learning for modeling, understanding, and controlling large-scale physics systems is quickly gaining in popularity, with examples ranging from electromagnetism over nuclear fusion reactors and magneto-hydrodynamics to fluid mechanics and climate modeling. These systems—governed by partial differential equations—present unique challenges regarding the large number of degrees of freedom and the complex dynamics over many scales both in space and time, and additional measures to improve accuracy and sample efficiency are highly desirable. We present an end-to-end equivariant surrogate model consisting of an equivariant convolutional autoencoder and an equivariant convolutional LSTM using G -steerable kernels. As a case study, we consider the three-dimensional Rayleigh-Bénard convection, which describes the buoyancy-driven fluid flow between a heated bottom and a cooled top plate. While the system is $E(2)$ -equivariant in the horizontal plane, the boundary conditions break the translational equivariance in the vertical direction. Our architecture leverages vertically stacked layers of D_4 -steerable kernels, with additional partial kernel sharing in the vertical direction for further efficiency improvement. Our results demonstrate significant gains both in sample and parameter efficiency, as well as a better scaling to more complex dynamics, that is, larger Rayleigh numbers. The accompanying code is available under <https://github.com/FynnFromme/equivariant-rb-forecasting>.

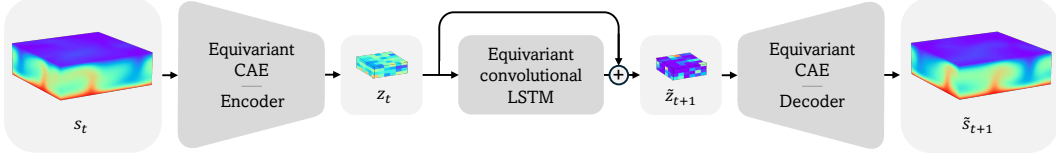


Figure 1: **Architecture overview.** (Left-right) An initial snapshot s_t is encoded via our E(2) equivariant 3D autoencoder to the latent representation z_t ; z_t is evolved forward in time to \tilde{z}_{t+1} via our equivariant LSTM; \tilde{z}_{t+1} is decoded via our E(2) equivariant 3D decoder to yield a predicted next snapshot \tilde{s}_{t+1} .

1 Introduction

The ability to perform fast and efficient simulations of large scale physics systems governed by partial differential equations (PDEs) is of vital importance in many areas of science and engineering. As in almost any other area, machine learning plays an increasingly important role, where scenarios of great interest are real-time prediction, uncertainty quantification, optimization and control. Application areas include weather forecasting [Kurth et al., 2023] and climate modeling [Vlachas et al., 2018], aerodynamics and fluid mechanics [Brunton et al., 2020], combustion [Ihme et al., 2022], or the plasma in nuclear fusion reactors [Kates-Harbeck et al., 2019]. PDE-governed systems often exhibit complex or chaotic behavior over a vast range of scales in both space and time. Along with the very large number of degrees of freedom (after discretization using, e.g., finite elements), this renders the resulting time series particularly challenging for surrogate modeling, especially in multi-query contexts such as prediction and control [Bieker et al., 2020]. Fortunately, many dynamical systems evolve on a low-dimensional manifold (e.g., an attractor), which allows for dimensionality reduction techniques and surrogate modeling. As linear approximation techniques such as proper orthogonal decomposition (POD) [Sirovich, 1987] tend to break down once the dynamics become more complex—as is the case for turbulent flows—nonlinear variants such as autoencoders have recently become more and more important in the physics modeling community [Nikolopoulos et al., 2022, Francés-Belda et al., 2024]. However, the resulting reduced spaces are less interpretable and the training is much more data-hungry and sensitive to hyperparameter tuning.

The goal of this paper is to include known symmetries in the surrogate modeling process of complicated 3D physics simulations via autoencoders. Studying a prototypical convection or climate system described as Rayleigh-Bénard convection, our contributions are the following (cf. Fig. 1 for a sketch):

- We develop an end-to-end equivariant architecture for the prediction of 3D time-dependent PDEs consisting of an autoencoder and an LSTM for time series prediction in latent space. To preserve the symmetry, we omit latent space flattening but preserve the original 3D structure of the problem.
- The system is equivariant under rotations, reflections and translations (i.e., the symmetry group $E(n)$), but only in the horizontal plane due to the buoyancy. We introduce an efficient G -steerable autoencoder architecture that respects the symmetry group $\mathbb{Z}^2 \rtimes D_4$ in the horizontal plane (the subgroup of $E(2)$ with shifts on a grid and discrete 90-degree rotations).
- Equivariance in the vertical direction is only broken by the boundary conditions (the equations themselves are equivariant under vertical translations). We incorporate additional local kernel sharing in the vertical direction and study its effects on performance and efficiency.
- We demonstrate high accuracy at a compression rate $> 98\%$, while saving one order of magnitude in both trainable parameters and training data compared to non-symmetric architectures.

2 Related work

Rayleigh-Bénard convection [Pandey et al., 2018] models the dynamics of a compressible fluid between two flat plates, where the bottom plate is heated while the top plate is cooled. This induces buoyancy forces which in turn result in fluid motion. At moderate Rayleigh numbers Ra (a dimensionless parameter quantifying the driving force induced by the temperature difference), one observes well-characterized convection rolls. With increasing Ra , the fluid becomes turbulent which

results in a large number of vortices on varying time and spatial scales, rendering the fluid hard to predict and characterize [Vieweg et al., 2021].

In recent years, a large number of works have appeared that address the task of **surrogate modeling** of PDE systems. Most of these approaches rely on the identification of a low-dimensional latent space for instance via POD [Soucasse et al., 2019], autoencoders [Pandey et al., 2022, Akbari et al., 2022, de Sousa Almeida et al., 2023] or simply random measurements [Gao et al., 2025] (even though the latter does not explicitly address Rayleigh-Bénard convection). Alternatively, the direct prediction of the full state can be accelerated using linear methods such as the Koopman operator framework [Klus et al., 2020, Markmann et al., 2024] or physics-informed machine learning [Karniadakis et al., 2021, Clark Di Leoni et al., 2023, Hammoud et al., 2023].

The **exploitation of symmetries** has recently become increasingly popular, and it is now often referred to under the umbrella term geometric deep learning [Bronstein et al., 2021]. Most of the literature in this area is until now related to classical learning tasks such as image classification [Cohen and Welling, 2016, Esteves et al., 2018a,b, Weiler and Cesa, 2019, Bronstein et al., 2021, Weiler et al., 2025]. However, equivariant architectures have been developed for various other tasks such as the analysis of graph-structured data (e.g., molecules [Wu et al., 2021]), or for the prediction of PDEs [Jenner and Weiler, 2022, Zhdanov et al., 2024, Harder et al., 2024b]. Equivariant autoencoder architectures for dimensionality reduction were proposed in, e.g., Kuzminykh et al. [2018], Guo et al. [2019], Huang et al. [2022], see also Hao et al. [2023], Yasuda and Onishi [2023] for applications to fluid flows. Further examples of equivariant learning of PDEs were presented in various contexts such as Koopman operator theory and Dynamic Mode Decomposition [Salova et al., 2019, Baddoo et al., 2023, Harder et al., 2024a, Peitz et al., 2025], as well as reinforcement learning [Vignon et al., 2023, Vasanth et al., 2024, Peitz et al., 2024, Jeon et al., 2024].

3 Preliminaries

Partial differential equations (PDEs) describe dynamical systems whose state s is a function of multiple variables such as space $x \in \Omega \subset \mathbb{R}^n$ and time $t \in \mathbb{R}^{\geq 0}$. The equations of motion are described by (nonlinear) partial differential operators,

$$\frac{\partial s}{\partial t} = \mathcal{F}(s, \nabla s, \Delta s, \dots) \quad \text{for } x \in \Omega, t \in \mathbb{R}^{\geq 0},$$

accompanied by appropriate boundary conditions on $\Gamma = \partial\Omega$ and initial conditions. In many cases, s is *equivariant* with respect to certain symmetry transformations such as translations or rotations.

3.1 Symmetries

We here give a very brief overview of symmetry groups and group actions, more detailed introductions can be found in, e.g., Weiler et al. [2021], Bronstein et al. [2021]. A group is a tuple (G, \circ) , where G is a set and $\circ : G \times G \rightarrow G, (g, h) \mapsto gh$ an operation which is associative, has an identity element e and inverses (denoted by g^{-1} for $g \in G$). The group operation describes the effect of chaining symmetry transformations. However, to employ group theory in practice, one needs an additional *object* that the group can *act on*. A *group action* is a function $G \times X \rightarrow X, (g, x) \mapsto g \cdot x$, where X is the underlying set of objects that are transformed. As for the group operation, one assumes associativity in the sense that $g \cdot (h \cdot x) = (gh) \cdot x$ together with invariance under the identity element.

A linear representation of G on a vector space V is a tuple (ρ, V) , where $\rho : G \rightarrow GL(V)$ is a group homomorphism from G to the general linear group $GL(V)$ of invertible linear maps of the vector space V , see [Weiler et al., 2021, Appendix B.5] for details. In case $V = \mathbb{R}^n$, the group action is defined as matrix multiplication by $\rho(g)$, i.e., $\rho(g) = A \in \mathbb{R}^{n \times n}, (g, x) \mapsto Ax$.

If a group action is defined on X , one can obtain an action on the space of functions of the form $\phi : X \rightarrow \mathbb{R}^m$ by introducing $(\rho(g)\phi)(x) := \phi(g^{-1} \cdot x)$. Here, we have already denoted the action as a representation, see [Cohen and Welling, 2017], as it is linear.

Example 1. The 2D Euclidean group $E(2)$ is the group of planar translations, rotations and reflections. It can be expressed as the semidirect product of translations $(\mathbb{R}^2, +)$ and orthogonal transformations, i.e., $E(2) = (\mathbb{R}^2, +) \rtimes O(2)$. A linear representation of $E(2)$ can be expressed as

$$E(2) = \left\{ \begin{pmatrix} A & \tau \\ 0 & 1 \end{pmatrix} \middle| A \in O(2), \tau \in \mathbb{R}^2 \right\}, \quad \text{with } O(2) = \{A \in \mathbb{R}^{2 \times 2} \mid A^\top A = Id\}.$$

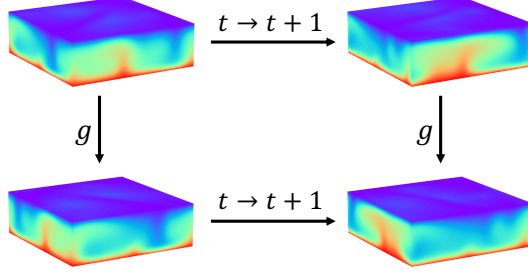


Figure 2: **Equivariance of time evolution and rotation.** The equivariance of the time evolution of the temperature field under a 90-degree rotation g is illustrated by the commutativity diagram.

An element $h \in E(2)$ can be decomposed into $h = \tau g$, where τ is a pure translation and g is a transformation that leaves the origin invariant.

In a straightforward manner, we can consider subgroups $H \leq E(2)$ when replacing $O(2)$ by a subgroup $G \leq O(2)$ and defining $H = (\mathbb{R}^2, +) \rtimes G$. When working with data on structured grids, as we do here, discrete translations and rotations can be implemented in a particularly efficient manner. This results in the dihedral group D_4 which allows for flips and 90-degree rotations. In combination with quantized translations on the grid nodes, we obtain $H = (\mathbb{Z}^2, +) \rtimes D_4 < E(2)$.

In general, for two sets X and Y , a function $\phi : X \rightarrow Y$ is called equivariant if there is a group acting both on X and Y such that $\phi(g \cdot x) = g \cdot \phi(x)$, or, equivalently, $\phi(x) = g^{-1} \cdot \phi(g \cdot x)$, for all $x \in X$ and $g \in G$. Intuitively, this means that one can obtain the result of $\phi(x)$ by first evaluating ϕ at the transformed object $g \cdot x$ and then applying the inverse transformation g^{-1} afterwards, cf. Fig. 2 for an illustration using the Rayleigh-Bénard system described in Section 3.2.

Convolutions. Conventional convolutions convolve a feature map $f_{\text{in}} : \mathbb{R}^n \rightarrow \mathbb{R}^{C_{\text{in}}}$ with a kernel $\psi : \mathbb{R}^n \rightarrow \mathbb{R}^{C_{\text{out}} \times C_{\text{in}}}$ as follows in order to produce a feature map $f_{\text{out}} : \mathbb{R}^n \rightarrow \mathbb{R}^{C_{\text{out}}}$:

$$f_{\text{out}}(x) = [f_{\text{in}} * \psi](x) = \int_{\mathbb{R}^n} \psi(x - y) f_{\text{in}}(y) dy$$

This is an example of a translation equivariant operation, as $[\rho(\tau) f_{\text{in}}] * \psi = \rho(\tau) [f_{\text{in}} * \psi]$ for $\tau \in \mathbb{R}^n$ [Cohen and Welling, 2016].

Steerable convolutions. In steerable CNNs, we define feature spaces in such a manner that the respective feature fields $f : \mathbb{R}^n \rightarrow \mathbb{R}^C$ are *steerable* [Cohen and Welling, 2017, Weiler and Cesa, 2019]. This means that for each n -dimensional input $x \in \mathbb{R}^n$, each C -dimensional feature $f(x) \in \mathbb{R}^C$ transforms under the group action of a given group G (e.g., $O(n)$)—the translational equivariance is automatically satisfied when the parameters of the learnable kernel ψ are position-independent [Weiler et al., 2021]. In particular, this ensures that the transformation of vector-valued features transforms their orientation according to the group action. As a consequence, all CNN architectures that are constructed using G -steerable kernels are equivariant with respect to the group $H = (\mathbb{R}^n, +) \rtimes G$. In Weiler and Cesa [2019], it was shown that for this property to hold, a kernel $\psi : \mathbb{R}^2 \rightarrow \mathbb{R}^{C_{\text{out}} \times C_{\text{in}}}$ has to satisfy the steerability constraint

$$\psi(g \cdot x) = \rho_{\text{out}}(g) \psi(x) \rho_{\text{in}}(g^{-1}) \quad \forall g \in G, x \in \mathbb{R}^2. \quad (1)$$

For a network to be equivariant, the kernel constraint (1) has to hold for all combinations of ρ_{in} and ρ_{out} . Instead, it is shown in Weiler and Cesa [2019] that a much simpler approach is to introduce a change of basis Q , by which any ρ can be decomposed into the direct sum of its irreducible representations (irreps), i.e., $\rho = Q^{-1} [\bigoplus_{i \in I} \psi_i] Q$. One can thus replace (1) by individual constraints on the irreps. Since we have $G \leq O(2)$, G is norm preserving, such that the kernel constraint can further be reformulated in terms of a Fourier series expansion of the kernel, ultimately resulting in a set of constraints on the Fourier coefficients, cf. Weiler and Cesa [2019], Weiler et al. [2021] for detailed derivations and discussions. We will make heavy use of this approach in our architecture, both in terms of the autoencoder and the LSTM for time series prediction.

3.2 Rayleigh-Bénard convection

Rayleigh-Bénard convection describes the flow between two flat plates. The bottom plate is heated, while the top plate is cooled, which induces buoyancy forces that cause the fluid to move in convection rolls, cf. Figs. 1 or 2 for illustrations. Depending on the driving force—the temperature difference, encoded by the dimensionless Rayleigh number Ra —the system is deterministic at first, then becomes increasingly complex and turbulent for larger Ra [Pandey et al., 2018].

For our simulation, we solve the so-called Boussinesq approximation of the compressible Navier-Stokes equations, where the fluid evolves according to the incompressible Navier-Stokes equations (continuity (2) and momentum (3)), even though the system is ultimately driven by an inhomogeneous density. Instead, the buoyancy force is modeled by a one-directional coupling with the energy conservation equation (4). In summary, we solve the following system of coupled PDEs in a rectangular domain $\Omega = (0, 2\pi) \times (0, 2\pi) \times (-1, 1)$ with periodic boundary conditions in the horizontal (i.e., first and second) directions and standard fixed walls boundary conditions with constant temperatures at the bottom and the top.

$$\nabla \cdot u = 0, \quad (2)$$

$$\frac{\partial u}{\partial t} + (u \cdot \nabla) u = \nabla p + \sqrt{\frac{Pr}{Ra}} \Delta u + Te_3, \quad (3)$$

$$\frac{\partial T}{\partial t} + u \cdot \nabla T = \frac{1}{\sqrt{RaPr}} \Delta T. \quad (4)$$

Here, $u(x, t) \in \mathbb{R}^3$ is the three-dimensional velocity (depending on space $x \in \Omega \subset \mathbb{R}^3$ and time $t \in \mathbb{R}^{\geq 0}$) and the scalar fields $p(x, t)$ and $T(x, t)$ denote the pressure and temperature, respectively. The canonical unit vector in the vertical direction is denoted as e_3 . The dimensionless numbers Ra and Pr are the Rayleigh and Prandtl numbers, respectively, cf. Pandey et al. [2018] for a more detailed description. The Prandtl number is a constant depending on the fluid properties (kinematic viscosity divided by thermal diffusivity), and we use the common value $Pr = 0.7$. We will study different values of Ra , which is the main influence factor in terms of the system complexity. For the numerical simulations to generate our training data, we have used the Julia code oceananigans.jl [Wagner et al., 2025], which introduces a finite volume discretization in the form of a grid with $N = N_1 \times N_2 \times N_3 = 48 \times 48 \times 32$ elements in space. These are equidistantly placed in all three directions so that we have a grid size of $\delta_1 = \delta_2 = 2\pi/48$ and $\delta_3 = 2/32$.

In the following, we will summarize the quantities of interest—temperature $T(x, t)$ and velocity $u(x, t)$, but not the pressure—in the state vector $s(x, t) \in \mathbb{R}^{C_{\text{in}}}$, where $C_{\text{in}} = 4$ is the number of input channels. Due to the discretization in space, the state function becomes a large tensor of dimension $N = N_1 \times N_2 \times N_3$. Moreover, we will consider snapshots at discrete times $t \in \mathbb{N}$, that is, $s_t = (u_t, T_t) \in \mathbb{R}^{N_1 \times N_2 \times N_3 \times C_{\text{in}}}$.

3.2.1 Symmetries of the 3D Rayleigh-Bénard convection system

The PDE we consider is a modification of the Navier-Stokes equations (NSE) with an additional temperature-dependent buoyancy term in the vertical direction. It is well-known that the 3D NSE are equivariant under actions of the symmetry group $E(3)$ [Olver, 1993, Wang et al., 2021]. Consequently, our system inherits the translational equivariance and $O(2)$ equivariance in the two horizontal directions, as only the vertical component of the momentum equation is altered. In addition, the translational symmetry in the vertical direction is broken by the fixed-temperature boundary conditions at the bottom and top. Locally, however, and sufficiently far away from the walls, equivariance should approximately hold, which we will exploit in our architecture. A more detailed discussion—including a proof—can be found in Appendix A.1.

4 Methods

Our framework comprises two main components: a convolutional autoencoder and a convolutional LSTM, trained independently. As illustrated in Fig. 1, the autoencoder first encodes a snapshot s_t into a latent representation z_t . The LSTM then sequentially forecasts subsequent latent representations $\tilde{z}_{t+1}, \tilde{z}_{t+2}, \dots$, which are subsequently decoded to full-state snapshots, $\tilde{s}_{t+1}, \tilde{s}_{t+2}, \dots$. Both the

autoencoder and LSTM are designed in an equivariant fashion. As a consequence, the entire framework is end-to-end equivariant.

4.1 3D steerable convolution on $E(2)$

As discussed in Section 3.2.1, the 3D Rayleigh-Bénard convection is $E(2)$ -equivariant in the horizontal plane, which we enforce by steerable convolutions, while introducing height-dependent kernels that adapt to the varying dynamics at different heights.

4.1.1 Steerable convolution

The system state s consists of both scalar temperature and vector-valued velocity fields. Under transformation of these fields by $\tau g \in E(2)$, the temperature field $T : \mathbb{R}^3 \rightarrow \mathbb{R}$ transforms as $T(x) \mapsto 1 \cdot T(g^{-1}(x - \tau))$, whereas the velocity-field $u : \mathbb{R}^3 \rightarrow \mathbb{R}^3$ transforms as $u(x) \mapsto g \cdot u(g^{-1}(x - \tau))$. Note that the velocity vectors are themselves transformed via g to preserve their orientation as the field is transformed Cohen and Welling [2017], Weiler and Cesa [2019].

To ensure equivariant mappings between three-dimensional feature fields $f_{\text{in}} : \mathbb{R}^3 \rightarrow \mathbb{R}^{C_{\text{in}}}$ and $f_{\text{out}} : \mathbb{R}^3 \rightarrow \mathbb{R}^{C_{\text{out}}}$, with corresponding transformations ρ_{in} and ρ_{out} , we constrain the kernels $\psi : \mathbb{R}^3 \rightarrow \mathbb{R}^{C_{\text{out}} \times C_{\text{in}}}$ to be $O(2)$ -steerable. Since the equivariance is restricted to the horizontal plane (i.e., x_1 and x_2) the group $O(2)$ acts on points x via the block-diagonal representation $\rho(g) = A \oplus 1$. The constraint can thus be decomposed into independent constraints for every fixed height \hat{x}_3 :

$$\psi \left(g \cdot \begin{pmatrix} x_1 \\ x_2 \\ \hat{x}_3 \end{pmatrix} \right) = \rho_{\text{out}}(g) \psi \left(\begin{pmatrix} x_1 \\ x_2 \\ \hat{x}_3 \end{pmatrix} \right) \rho_{\text{in}}(g^{-1}) \quad \forall g \in O(2), \begin{pmatrix} x_1 \\ x_2 \\ \hat{x}_3 \end{pmatrix} \in \mathbb{R}^3. \quad (5)$$

Thus, a three-dimensional $O(2)$ -steerable kernel can be constructed as a stack of 2D $O(2)$ -steerable kernels. For these, Weiler and Cesa [2019] have solved the steerability constraint as well as for important subgroups such as C_4 and D_4 . This result has been applied in our implementation to efficiently design height-dependent kernels utilizing the PyTorch-based library `escnn`.¹ For computational reasons, we restrict our implementation to the subgroup $H = (\mathbb{Z}^2, +) \rtimes D_4 < E(2)$, as this optimally corresponds to our data on a rectangular grid. Thus, we will from now on consider discretized kernels and feature fields on \mathbb{Z}^3 . The case of continuous rotations according to $O(2)$ would require interpolation between grid points (see, e.g., Esteves et al. [2018a]). In our experiments, this resulted in inferior performance compared to the grid-consistent 90-degree-rotations and flips.

Within our framework, we use various types of feature fields. Both the input to the AE-encoder and the output of the decoder are composed of the scalar field T and the vector field u . All intermediate representations, however, make use of regular feature fields, which transform under the regular representation by permuting the channels. Steerable convolutions between regular feature fields are equivalent to regular group convolutions [Cohen and Welling, 2016], which apply the same kernel in every orientation $g \in G$, resulting in the $|G|$ -dimensional regular feature fields.

4.1.2 3D convolutions with height-dependent kernels

Height-dependent features—such as temperature or velocity patterns—play a critical role in modeling the system. As a result, applying the same kernel across all heights—as would be the case for a regular 3D CNN—is insufficient to capture the system’s vertical dynamics. To address this limitation, we modify the conventional 3D convolutions by learning height-dependent steerable kernels. While this ensures horizontal parameter sharing, we allow the convolution operation to adapt to the distinct features at each height, ensuring that the vertical structure is captured effectively. For computing the output feature map’s value at position $x = (x_1, x_2, x_3) \in \mathbb{Z}^3$, the input $f : \mathbb{Z}^3 \rightarrow \mathbb{R}^{C_{\text{in}}}$ is convolved with the height-dependent kernel $\psi_{x_3} : \mathbb{Z}^3 \rightarrow \mathbb{R}^{C_{\text{out}} \times C_{\text{in}}}$ via $[f * \psi](x) = \sum_{y \in \mathbb{Z}^3} \psi_{x_3}(x - y) f(y)$.

Local vertical parameter sharing. Although the Rayleigh-Bénard system does not exhibit global vertical translation equivariance, it approximately maintains this property within a local neighborhood (see Section 3.2.1). This suggests that features at a given height x_3 are locally correlated with features at vertical positions within a $2k + 1$ -sized neighborhood $\mathcal{N}(x_3) = \{x_3 - k, \dots, x_3 + k\}$. This approximate local equivariance in the vertical direction can be exploited by choosing a smaller number

¹<https://github.com/QUVA-Lab/escnn>

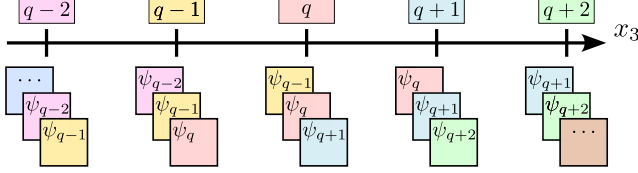


Figure 3: **Local vertical kernel sharing.** Kernels of different heights $\hat{x}_3 = q - 2, q - 1, q, \dots$ are applied to the neighboring $k = 1$ heights, resulting in a total of 3 kernels being applied each.

of channels in each layer, but then applying these learned kernels across the local neighborhood \mathcal{N} , thereby again increasing the number of output channels, cf. Fig. 3 for a sketch. This parameter reduction leads to a more efficient and scalable model, rendering it suitable for simulating larger-scale systems. As described in Appendix A.2, 3D convolutions with height-dependent kernels and local vertical parameter sharing can be efficiently implemented by wrapping 2D (steerable) convolutions.

4.2 Equivariant autoencoder

The convolutional autoencoder (CAE) is designed to respect the horizontal $E(2)$ symmetry by incorporating equivariant convolutions into both the encoder and decoder. In the encoder, an input snapshot s_t of shape $N_1 \times N_2 \times N_3 \times C_{\text{in}}$ is mapped to a lower-dimensional latent representation z_t of shape $M_1 \times M_2 \times M_3 \times C_{\text{latent}}$, through a sequence of convolutional layers progressively extracting higher-level features. Each layer is followed by activation functions and max-pooling. Notably—instead of the common flattening—the latent space maintains the systems original spatial structure to preserve spatial correlations in the data, although we have $M \ll N$. The number of channels C_{latent} is used to control the size and expressiveness of the latent representation.

The decoder applies a series of convolutions, followed by activation functions. Pooling operations are replaced by upsampling. To preserve continuity while upsampling, we employ trilinear interpolation. Throughout the entire framework (CAE + LSTM), padding is applied to the convolutional layers to ensure that the spatial dimensions of the data are only altered by pooling and upsampling operations. For the horizontal dimensions, circular padding is used to match the periodic boundary conditions of the Rayleigh-Bénard system, while vertical dimensions use zero padding. Note that without padding, the decoder would require transposed convolutions [Dumoulin and Visin, 2018] to reverse the dimensional changes induced by convolutions without padding.

4.3 Equivariant LSTM

Long short-term memory (LSTM) networks [Hochreiter and Schmidhuber, 1997] extend conventional recurrent neural networks (RNNs) for processing sequential data by an additional cell state c_t . While the hidden state h_t stores currently relevant information for predicting the next time step, the cell state c_t captures long-term information over long sequences. The content of c_t is regulated by the input gate i_t , which controls which information is added, and the forget gate f_t , which controls how much information is discarded. The output gate o_t determines which information is passed from h_t to c_t . To preserve the spatial structure of the latent space z , we use convolutional LSTMs [Shi et al., 2015] that replace the fully connected layers of standard LSTMs with, in our case, equivariant convolutions and also introduce equivariant convolutions in peephole connections. The equations are defined as follows:

$$\begin{aligned}
 i_t &= \sigma(z_t * \psi^{zi} + h_{t-1} * \psi^{hi} + c_{t-1} * \psi^{ci} + b_i) \\
 f_t &= \sigma(z_t * \psi^{zf} + h_{t-1} * \psi^{hf} + c_{t-1} * \psi^{cf} + b_f) \\
 c_t &= f_t \odot c_{t-1} + i_t \odot \tanh(z_t * \psi^{zc} + h_{t-1} * \psi^{hc} + b_c) \\
 o_t &= \sigma(z_t * \psi^{zo} + h_{t-1} * \psi^{ho} + c_t * \psi^{co} + b_o) \\
 h_t &= o_t \odot \tanh(c_t)
 \end{aligned}$$

Here, we use peephole connections, where the cell state is included in the gates to control the information entering and leaving the cell state more accurately. Replacing the Hadamard products of traditional peephole connections with convolutions ensures that the LSTM remains equivariant,

as shown below. Notably, this approach also resolves the issue of exploding gradients we initially observed in our experiments when using a standard 3D convolutional LSTM without convolutional peephole connections.

The new latent representation z_{t+1} is predicted based on the current hidden state via

$$z_{t+1} = z_t + h_t * \psi + b.$$

The output z_{t+1} of the current time step is then used as the input for the next time step, allowing the model to autoregressively forecast future states.

Equivariance of the LSTM system dynamics. The LSTM can be seen as modeling a dynamical system of the form

$$(z_t, c_{t-1}, h_{t-1}) \mapsto (z_{t+1}, c_t, h_t), \quad (6)$$

where the remaining variables i_t, f_t and o_t can be computed solely from z_t, c_{t-1}, h_{t-1} . Equivariance in this context means that a transformed input yields a transformed output, i.e.,

$$(\rho(g)z_t, \rho(g)c_{t-1}, \rho(g)h_{t-1}) \mapsto (\rho(g)z_{t+1}, \rho(g)c_t, \rho(g)h_t). \quad (7)$$

It follows from three facts, all due to Weiler and Cesa [2019]: Firstly, convolutions are equivariant in the sense that $\rho(g)\ell * \psi = \rho(g)(\ell * \psi)$ for an arbitrary feature map ℓ . Secondly, the action is linear, i.e., $\rho(g)\ell + \rho(g)\ell' = \rho(g)(\ell + \ell')$. And thirdly, it satisfies $\sigma(\rho(g)\ell) = \rho(g)\sigma(\ell)$ whenever σ is a pointwise function. Since all feature maps are transformed jointly, the Hadamard product is equivariant too, i.e., $\rho(g)\ell \odot \rho(g)\ell' = \rho(g)(\ell \odot \ell')$.

End-to-end equivariance of the entire architecture then simply follows from the observation that all CAE as well as all LSTM layers are equivariant w.r.t. the same symmetry group.

5 Experiments

We compare the performance of our end-to-end equivariant framework to a similar-in-size baseline model using standard, non-steerable 3D convolutions, with a particular focus on the autoencoder.

Datasets. We generated a dataset of 100 randomly initialized 3D Rayleigh-Bénard convection simulations with $Ra = 2500$ and $Pr = 0.7$, standardized to zero mean and unit standard deviation. The dataset was split into 60 training, 20 validation, and 20 test simulations, each with 400 snapshots in the time interval $t \in [100, 300]$ at a step size of 0.5 and a spatial resolution of $N = 48 \times 48 \times 32$. For long-term forecasting evaluation, we also created an additional dataset of 20 simulations, each containing 1800 snapshots over $t \in [100, 1000]$.

Architecture. The CAE encoder and decoder each consist of six convolutional layers with a kernel size of three for the last encoder and first decoder layer, and five for the other layers, applying ELU nonlinearities pointwise.² Pooling and upsampling are applied after the encoder and decoder's first, third, and fifth layers, respectively. The latent space has dimensions $M = 6 \times 6 \times 4$ and $C_{\text{latent}} = 32$ channels, resulting in a compression to 1.56% of the original size. Channels roughly double after each pooling operation in the encoder, with the decoder reversing this. Over our experiments, we vary the channel sizes. For a fair comparison, our main models (both standard and equivariant) have approximately the same number of 3.6M parameters. The decoder-only LSTM with one layer of convolutional LSTM cells and an additional convolutional layer for output prediction uses a kernel size of 3. The number of channels is chosen such that the LSTM has approximately 3.7M parameters.

Training. CAE training is performed in the standard self-supervised manner on a set of snapshots, where the desired decoder-output is the original input. The LSTM was then trained on the latent representations to predict the 50 latent states following the provided sequence of 25 states, with the loss being computed on the latent space. This two-step training approach effectively separates encoding and forecasting, avoiding significant performance drops. Mixing them leads to poor results, as the LSTM output (the latent representation) is autoregressively fed back into the model without intermediate decoding and encoding. Consequently, end-to-end fine-tuning resulted in suboptimal forecasting performance. For more training details, cf. A.3.

²All hidden layers in our model transform under the regular representation, which preserves equivariance since it commutes with pointwise nonlinearities [Weiler and Cesa, 2019].

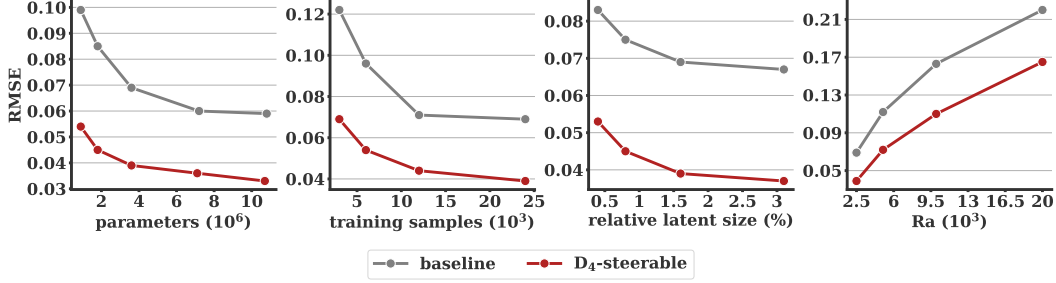


Figure 4: **CAE performances.** Results are shown with varying numbers of parameters, amounts of training samples, compression ratios, and Rayleigh numbers Ra . Each plot shows a variation over one of the parameters while keeping the others fixed. The main model has 3.6 million parameters (3rd point), 24,000 training samples (4th point), 1.56% latent size (3rd point) and $Ra = 2500$ (1st point).

5.1 Results

We begin with a detailed evaluation of the CAE performance, followed by an analysis of the long-term forecasting capability of our end-to-end equivariant model.

Autoencoder. Fig. 4 gives an overview of our experiments to compare the equivariant and baseline architectures with respect to parameter efficiency, data efficiency, compression capabilities and scalability to more complex dynamics, i.e., larger Ra . Equivariance leads to a significant improvement in reconstruction accuracy, with the RMSE decreasing by 42%, from 0.069 ± 0.00072 to 0.04 ± 0.00093 , where the mean and standard deviation were computed across three models with randomly initialized weights. A comparison to C_4 -equivariant convolutions shows an RMSE of 0.046 ± 0.00164 , showing that both rotations and reflections are relevant for the improved performance.

When studying the four subfigures separately, we observe several significant advantages of incorporating equivariance:

- (i) **Parameter efficiency:** The equivariant model with only 900,000 parameters outperformed the baseline model with 10.8 million parameters, meaning that we obtain an improvement by more than one order of magnitude.
- (ii) **Sample efficiency:** The D_4 model achieved the same performance as the baseline when trained on just one-eighth of the training samples, representing a significant reduction in the amount of data required for effective learning, making it particularly valuable in data-limited scenarios or when simulations/experiments are expensive.
- (iii) **Compression capabilities:** Even when increasing the compression ratio by a factor of eight, the equivariant model has significantly superior accuracy. This is particularly important when dealing with large-scale systems, as well as for consecutive learning tasks such as training the LSTM.
- (iv) **Scaling to complex dynamics:** When increasing the Rayleigh number Ra from 2,500 up to 20,000, we observe that the gap in accuracy even increases further, which indicates that the equivariant model is better equipped to handle more complex dynamics. This suggests that incorporating equivariance into the architecture allows the model to better capture and represent complex fluid flow dynamics inherent in the Rayleigh-Bénard convection system, in particular as the patterns grow more complex.

The results discussed so far have been obtained without local parameter sharing in the vertical direction. Our experiments with local vertical sharing show only minor improvements over the results in Fig. 4. However, we have considered a fairly moderate number of $N_3 = 32$ vertical layers for now. The results thus merely show that vertical parameter sharing is viable, and we believe that it will become significantly more relevant when considering setups with even larger state spaces. In these situations, learning entirely separate features for each height will become computationally infeasible. A detailed assessment for much larger state spaces will be the focus of future work.

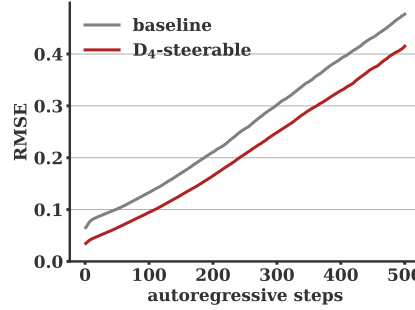


Figure 5: **Forecasting RMSE.** For each of three randomly initialized models, the median forecasting RMSE was computed over a time horizon of 500. We present the average of these medians.

Long-term forecasting. We next focus on the evaluation of the long-term forecasting capabilities of our end-to-end equivariant architecture. The model is provided with an input sequence of 50 snapshots and then predicts the subsequent 500 future states in an autoregressive manner, i.e., using its own predictions as input for the next time step.

Fig. 5 shows the median RMSE over time for both the equivariant and baseline model, which was averaged over three separately trained models. The equivariant model consistently outperforms the baseline by a near-constant margin of approximately 0.05 RMSE across the entire forecast horizon. This indicates that most of the performance gains stem from improved latent representation learned by the equivariant autoencoder, which provides a more stable and informative basis for prediction.

Qualitative examples in Fig. 6 further highlight the performance of our surrogate model. The equivariant model is able to preserve the fine-scale structures and large-scale convective patterns over extended time periods. Only minor spatial displacements of the convective plumes are observed, even after hundreds of time steps.

6 Conclusion

We have developed an end-to-end equivariant CAE plus LSTM architecture for efficient surrogate modeling of 3D Rayleigh-Bénard convection, which includes horizontally $E(2)$ -equivariant kernels that are vertically stacked. Additional local sharing in the vertical direction allows us to increase the number of channels without requiring additional parameters, which further adds to the computational

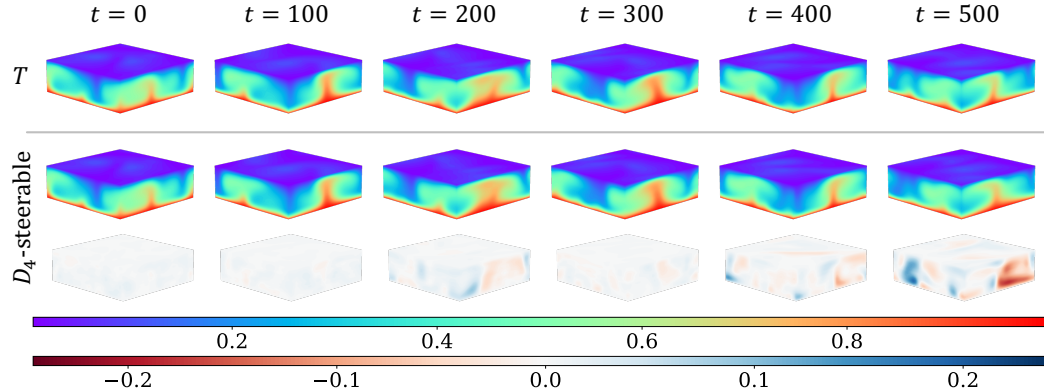


Figure 6: **Representative autoregressive forecast.** The top row displays the ground truth temperature field T at selected time steps t . The middle row shows the predictions by the equivariant surrogate model (at $t = 0$, we show CAE reconstruction (encoding + decoding) of the ground truth). The bottom row represents the difference between the predicted and ground truth temperature fields.

efficiency. We have demonstrated significant advantages in terms of the accuracy and both data and parameter efficiency.

6.1 Limitations and outlook

There are still several limitations that we have not yet discussed or addressed, but believe to be important and fruitful for future research

- We have used idealized simulations without noise or other symmetry-breaking disturbances; this will be essential for studying the robustness in real-world settings.
- Instead of the sequential training approach, an end-to-end training could be superior, since the latent representation is tailored to the dynamics; since this proved to be challenging for LSTMs, an alternative could be linear models based on the Koopman operator [Harder et al., 2024a], which has proven to be a powerful tool for learning dynamical systems, also in combination with autoencoders [Otto and Rowley, 2019].
- In the control setting, equivariant models are very helpful to improve the efficiency, for instance of world models in the context of reinforcement learning; surrogate modeling for RL of PDEs was studied in, e.g., Werner and Peitz [2024], but a combination with equivariant RL as proposed in van der Pol et al. [2020] has not been investigated.
- For climate applications, equivariant models on spheres would be very interesting to study (cf., e.g., Gastine et al. [2015] for a spherical Rayleigh–Bénard case); besides additional challenges in terms of the numerical implementation, the rotation of the earth would also result in fewer symmetries, such that the usefulness of equivariant models has yet to be determined.

Code

The accompanying code is available under <https://github.com/FynnFromme/equivariant-rb-forecasting>.

Acknowledgments

FF acknowledges support by the German Federal Ministry of Education and Research (BMBF) within the AI junior research group “Multicriteria Machine Learning”. HH acknowledges support by the project “SAIL: SustAInable Lifecycle of Intelligent Socio-Technical Systems” (Grant ID NW21-059D), funded by the Ministry of Culture and Science of the State of Northrhine Westphalia (NRW), Germany. SP acknowledges support by the European Union via the ERC Starting Grant “KoOpeRaDE” (Grant ID 101161457). The calculations have been performed on Hardware funded by BMBF and NRW as part of the Lamarr Institute for Machine Learning and Artificial Intelligence.

References

S. Akbari, S. Pawar, and O. S. and. Numerical assessment of a nonintrusive surrogate model based on recurrent neural networks and proper orthogonal decomposition: Rayleigh–Bénard convection. *International Journal of Computational Fluid Dynamics*, 36(7):599–617, 2022.

P. J. Baddoo, B. Herrmann, B. J. McKeon, J. Nathan Kutz, and S. L. Brunton. Physics-informed dynamic mode decomposition. *Proceedings of the Royal Society A: Mathematical, Physical and Engineering Sciences*, 479(2271):20220576, 2023.

S. Bengio, O. Vinyals, N. Jaitly, and N. Shazeer. Scheduled Sampling for Sequence Prediction with Recurrent Neural Networks, Sept. 2015.

K. Bieker, S. Peitz, S. L. Brunton, J. N. Kutz, and M. Dellnitz. Deep model predictive flow control with limited sensor data and online learning. *Theoretical and Computational Fluid Dynamics*, 34: 577–591, 2020.

M. M. Bronstein, J. Bruna, T. Cohen, and P. Veličković. Geometric deep learning: Grids, groups, graphs, geodesics, and gauges. *arXiv:2104.13478*, 4 2021.

S. L. Brunton, B. R. Noack, and P. Koumoutsakos. Machine learning for fluid mechanics. *Annual Review of Fluid Mechanics*, 52:477–508, 2020. doi: <https://doi.org/10.1146/annurev-fluid-010719-060214>.

P. Clark Di Leoni, L. Agasthya, M. Buzzicotti, and L. Biferale. Reconstructing Rayleigh–Bénard flows out of temperature-only measurements using physics-informed neural networks. *The European Physical Journal E*, 46(3), Mar. 2023. ISSN 1292-895X. doi: 10.1140/epje/s10189-023-00276-9. URL <http://dx.doi.org/10.1140/epje/s10189-023-00276-9>.

T. S. Cohen and M. Welling. Group equivariant convolutional networks. In *International Conference on Machine Learning*, 2016.

T. S. Cohen and M. Welling. Steerable CNNs. In *Proceedings of the International Conference on Learning Representations*, 2017.

J. L. de Sousa Almeida, P. R. Barbosa Rocha, A. M. de Carvalho, and A. Costa Nogueira Jr. A coupled variational encoder-decoder - deepONet surrogate model for the Rayleigh–Bénard convection problem. In *When Machine Learning meets Dynamical Systems: Theory and Applications*, 2023.

V. Dumoulin and F. Visin. A guide to convolution arithmetic for deep learning, Jan. 2018.

C. Esteves, C. Allen-Blanchette, A. Makadia, and K. Daniilidis. Learning SO(3) equivariant representations with spherical CNNs. In *European Conference on Computer Vision*, 2018a.

C. Esteves, C. Allen-Blanchette, X. Zhou, and K. Daniilidis. Polar transformer networks. In *International Conference on Learning Representations*, 2018b.

V. Francés-Belda, A. Solera-Rico, J. Nieto-Centenero, E. Andrés, C. Sanmiguel Vila, and R. Castellanos. Toward aerodynamic surrogate modeling based on β -variational autoencoders. *Physics of Fluids*, 36(11), Nov. 2024. ISSN 1089-7666. doi: 10.1063/5.0232644. URL <http://dx.doi.org/10.1063/5.0232644>.

M. L. Gao, J. P. Williams, and J. N. Kutz. Sparse identification of nonlinear dynamics and koopman operators with shallow recurrent decoder networks. *arXiv:2501.13329*, 2025.

T. Gastine, J. Wicht, and J. M. Aurnou. Turbulent rayleigh–bénard convection in spherical shells. *Journal of Fluid Mechanics*, 778:721–764, 2015.

X. Guo, E. Zhu, X. Liu, and J. Yin. Affine equivariant autoencoder. In *Proceedings of the 28th International Joint Conference on Artificial Intelligence (IJCAI-19)*, pages 2413–2419. International Joint Conferences on Artificial Intelligence Organization, 2019.

M. A. E. R. Hammoud, H. Alwassel, B. Ghanem, O. Knio, and I. Hoteit. Physics-informed deep neural network for backward-in-time prediction: Application to Rayleigh–Bénard convection. *Artificial Intelligence for the Earth Systems*, 2(1), Jan. 2023. ISSN 2769-7525. doi: 10.1175/aiies-d-22-0076.1. URL <http://dx.doi.org/10.1175/AIES-D-22-0076.1>.

Z. Hao, R. Kansal, J. Duarte, and N. Chernyavskaya. Lorentz group equivariant autoencoders. *The European Physical Journal C*, 83(6):485, 2023.

H. Harder, S. Peitz, F. Nüske, F. Philipp, M. Schaller, and K. Worthmann. Group convolutional extended dynamic mode decomposition. *arXiv:2411.00905*, 2024a.

H. Harder, J. Rabault, R. Vinuesa, M. Mortensen, and S. Peitz. Solving partial differential equations with equivariant extreme learning machines. *arXiv:2404.18530*, 2024b.

S. Hochreiter and J. Schmidhuber. Long Short-Term Memory. *Neural Computation*, 9(8):1735–1780, Nov. 1997. ISSN 0899-7667. doi: 10.1162/neco.1997.9.8.1735.

Y. Huang, X. Peng, J. Ma, and M. Zhang. 3DLinker: An E(3) equivariant variational autoencoder for molecular linker design. *arXiv:2205.07309*, 2022.

M. Ihme, W. T. Chung, and A. A. Mishra. Combustion machine learning: Principles, progress and prospects. *Progress in Energy and Combustion Science*, 91:101010, 2022. ISSN 0360-1285. doi: <https://doi.org/10.1016/j.pecs.2022.101010>. URL <https://www.sciencedirect.com/science/article/pii/S0360128522000193>.

E. Jenner and M. Weiler. Steerable partial differential operators for equivariant neural networks. In *International Conference on Learning Representations (ICLR)*, 2022.

J. Jeon, J. Rabault, J. Vasanth, F. Alcántara-Ávila, S. Baral, and R. Vinuesa. Advanced deep-reinforcement-learning methods for flow control: group-invariant and positional-encoding networks improve learning speed and quality. *arXiv:2407.17822*, 2024. URL <https://arxiv.org/abs/2407.17822>.

G. E. Karniadakis, I. G. Kevrekidis, L. Lu, P. Perdikaris, S. Wang, and L. Yang. Physics-informed machine learning. *Nature Reviews Physics*, 3(6):422–440, 2021.

J. Kates-Harbeck, A. Svyatkovskiy, and W. Tang. Predicting disruptive instabilities in controlled fusion plasmas through deep learning. *Nature*, 568(7753):526–531, Apr. 2019. ISSN 1476-4687. doi: 10.1038/s41586-019-1116-4. URL <http://dx.doi.org/10.1038/s41586-019-1116-4>.

D. P. Kingma and J. Ba. Adam: A Method for Stochastic Optimization, Jan. 2017.

S. Klus, F. Nüske, S. Peitz, J.-H. Niemann, C. Clementi, and C. Schütte. Data-driven approximation of the Koopman generator: Model reduction, system identification, and control. *Physica D: Nonlinear Phenomena*, 406:132416, 2020.

T. Kurth, S. Subramanian, P. Harrington, J. Pathak, M. Mardani, D. Hall, A. Miele, K. Kashinath, and A. Anandkumar. Fourcastnet: Accelerating global high-resolution weather forecasting using adaptive Fourier neural operators. In *Proceedings of the Platform for Advanced Scientific Computing Conference*, PASC ’23, New York, NY, USA, 2023. Association for Computing Machinery. ISBN 9798400701900. doi: 10.1145/3592979.3593412. URL <https://doi.org/10.1145/3592979.3593412>.

D. Kuzminikh, D. Polykovskiy, and A. Zhebrak. Extracting invariant features from images using an equivariant autoencoder. In J. Zhu and I. Takeuchi, editors, *Proceedings of The 10th Asian Conference on Machine Learning*, volume 95 of *Proceedings of Machine Learning Research*, pages 438–453. PMLR, 14–16 Nov 2018.

T. Markmann, M. Straat, and B. Hammer. Koopman-based surrogate modelling of turbulent Rayleigh-Bénard convection. In *2024 International Joint Conference on Neural Networks (IJCNN)*, pages 1–8, 2024.

S. Nikolopoulos, I. Kalogeris, and V. Papadopoulos. Non-intrusive surrogate modeling for parametrized time-dependent partial differential equations using convolutional autoencoders. *Engineering Applications of Artificial Intelligence*, 109:104652, Mar. 2022. ISSN 0952-1976. doi: 10.1016/j.engappai.2021.104652. URL <http://dx.doi.org/10.1016/j.engappai.2021.104652>.

P. J. Olver. *Applications of Lie Groups to Differential Equations*. Springer New York, 1993.

S. E. Otto and C. W. Rowley. Linearly recurrent autoencoder networks for learning dynamics. *SIAM Journal on Applied Dynamical Systems*, 18(1):558–593, 2019. doi: 10.1137/18M1177846.

A. Pandey, J. D. Scheel, and J. Schumacher. Turbulent superstructures in Rayleigh-Bénard convection. *Nature Communications*, 9(1):2118, 2018.

S. Pandey, P. Teutsch, P. Mäder, and J. Schumacher. Direct data-driven forecast of local turbulent heat flux in Rayleigh-Bénard convection. *Physics of Fluids*, 34(4):045106, 2022.

S. Peitz, J. Stenner, V. Chidananda, O. Wallscheid, S. L. Brunton, and K. Taira. Distributed control of partial differential equations using convolutional reinforcement learning. *Physica D: Nonlinear Phenomena*, 461:134096, 2024.

S. Peitz, H. Harder, F. Nüske, F. M. Philipp, M. Schaller, and K. Worthmann. Equivariance and partial observations in Koopman operator theory for partial differential equations. *Journal of Computational Dynamics*, 12:305–324, 2025.

A. Salova, J. Emenheiser, A. Rupe, J. P. Crutchfield, and R. M. D’Souza. Koopman operator and its approximations for systems with symmetries. *Chaos: An Interdisciplinary Journal of Nonlinear Science*, 29:093128, 9 2019.

X. Shi, Z. Chen, H. Wang, D.-Y. Yeung, W.-k. Wong, and W.-c. WOO. Convolutional LSTM network: A machine learning approach for precipitation nowcasting. In *Advances in Neural Information Processing Systems*, volume 28. Curran Associates, Inc., 2015.

L. Sirovich. Turbulence and the dynamics of coherent structures part I: coherent structures. *Quarterly of Applied Mathematics*, XLV(3):561–571, 1987.

L. Soucasse, B. Podvin, P. Rivière, and A. Soufiani. Proper orthogonal decomposition analysis and modelling of large-scale flow reorientations in a cubic Rayleigh–Bénard cell. *Journal of Fluid Mechanics*, 881:23–50, 2019. doi: 10.1017/jfm.2019.746.

E. van der Pol, D. E. Worrall, H. van Hoof, F. A. Oliehoek, and M. Welling. MDP homomorphic networks: Group symmetries in reinforcement learning. In *34th Conference on Neural Information Processing Systems*, 2020.

J. Vasanth, J. Rabault, F. Alcántara-Ávila, M. Mortensen, and R. Vinuesa. Multi-agent reinforcement learning for the control of three-dimensional Rayleigh–Bénard convection. *Flow, Turbulence and Combustion*, 2024.

P. P. Vieweg, C. Schneide, K. Padberg-Gehle, and J. Schumacher. Lagrangian heat transport in turbulent three-dimensional convection. *Phys. Rev. Fluids*, 6:L041501, Apr 2021.

C. Vignon, J. Rabault, J. Vasanth, F. Alcántara-Ávila, M. Mortensen, and R. Vinuesa. Effective control of two-dimensional Rayleigh–Bénard convection: Invariant multi-agent reinforcement learning is all you need. *Physics of Fluids*, 35(6):065146, 2023.

P. R. Vlachas, W. Byeon, Z. Y. Wan, T. P. Sapsis, and P. Koumoutsakos. Data-driven forecasting of high-dimensional chaotic systems with long short-term memory networks. *Proceedings of the Royal Society A: Mathematical, Physical and Engineering Sciences*, 474, 2018. ISSN 14712946. doi: 10.1098/rspa.2017.0844.

G. L. Wagner, S. Silvestri, N. C. Constantinou, A. Ramadhan, J.-M. Campin, C. Hill, T. Chor, J. Strong-Wright, X. K. Lee, F. Poulin, A. Souza, K. J. Burns, J. Marshall, and R. Ferrari. High-level, high-resolution ocean modeling at all scales with Oceananigans. *arXiv:2502.14148*, 2025.

R. Wang, R. Walters, and R. Yu. Incorporating symmetry into deep dynamics models for improved generalization. In *International Conference on Learning Representations*, 2021.

M. Weiler and G. Cesa. General $E(2)$ -equivariant steerable CNNs. In H. Wallach, H. Larochelle, A. Beygelzimer, F. d’Alché-Buc, E. Fox, and R. Garnett, editors, *Advances in Neural Information Processing Systems*, volume 32, 2019.

M. Weiler, P. Forré, E. Verlinde, and M. Welling. Coordinate independent convolutional networks: Isometry and gauge equivariant convolutions on riemannian manifolds. *arXiv:2106.06020*, 2021.

M. Weiler, P. Forré, E. Verlinde, and M. Welling. *Equivariant and Coordinate Independent Convolutional Networks*. Progress in Data Science: Volume 1. World Scientific, 2025. doi: 10.1142/14143.

S. Werner and S. Peitz. Numerical evidence for sample efficiency of model-based over model-free reinforcement learning control of partial differential equations. In *European Control Conference (ECC)*, pages 2958–2964. IEEE, 2024.

Z. Wu, S. Pan, F. Chen, G. Long, C. Zhang, and P. S. Yu. A comprehensive survey on graph neural networks. *IEEE Transactions on Neural Networks and Learning Systems*, 32(1):4–24, 2021.

Y. Yasuda and R. Onishi. Rotationally equivariant super-resolution of velocity fields in two-dimensional flows using convolutional neural networks. *APL Machine Learning*, 1(2):026107, 2023.

M. Zhdanov, D. Ruhe, M. Weiler, A. Lucic, J. Brandstetter, and P. Forré. Clifford-steerable convolutional neural networks. In *Forty-first International Conference on Machine Learning*, 2024.

A Appendix

A.1 Symmetries in the Rayleigh-Bénard system

The symmetries described in Section 3.2.1 can be formalized as equivariance with respect to three-dimensional rigid transformations $R(x) = Ax + b$, where A leaves the vertical direction invariant, i.e., it has a 2×2 orthogonal block in the top-left corner and acts like the identity in the third (= the vertical) dimension. Together with function composition as the operation, the set of these rigid transformations yields a group (G, \circ) .

An action of G on scalar fields is simply defined via function composition, that is, by rotating or translating the underlying coordinate domain. This action is extended to vector- or tensor-fields, but here we have to transform their components too:

- For a scalar field $s : \mathbb{R}^3 \rightarrow \mathbb{R}$, a group action is defined by $R \cdot s = s \circ R$.
- For a vector field $v : \mathbb{R}^3 \rightarrow \mathbb{R}^3$, a group action is defined by $R \cdot v = A^\top v \circ R$.
- For a tensor field $M : \mathbb{R}^3 \rightarrow \mathbb{R}^{3 \times 3}$, a group action is defined by $R \cdot M = A^\top M A \circ R$.

From these definitions, equivariance of the Rayleigh-Bénard convection holds in the following sense: Writing equations (3) and (4) as $u_t = f(u, T, p)$ and $T_t = g(u, T, p)$, it holds that

$$u_t = R^{-1} \cdot f(R \cdot u, R \cdot T, R \cdot p) \quad \text{and} \quad T_t = R^{-1} \cdot g(R \cdot u, R \cdot T, R \cdot p). \quad (8)$$

Proof. We have

$$u_t = f(u, T, p) = -(\nabla u)^\top u + \nabla p + \sqrt{\frac{Pr}{Ra}} \Delta u + Te_3,$$

$$T_t = g(u, T, p) = -(\nabla T)^\top u + \frac{1}{\sqrt{RaPr}} \Delta T.$$

To treat vector fields consistently in column format, we have written $u \cdot \nabla u$ in (3) and $u \cdot \nabla T$ in (4) as $(\nabla u)^\top u$ and $(\nabla T)^\top u$, respectively.

We state the following vector calculus identities without proof, but note that they follow from straight-forward calculations:

$$\nabla(R \cdot w) = R \cdot \nabla w, \quad (\text{for } w \text{ a scalar or vector field}) \quad (9)$$

$$\nabla(R \cdot w) = R \cdot \nabla w, \quad (\text{for } w \text{ a scalar or vector field}) \quad (10)$$

$$\nabla \cdot (R \cdot w) = R \cdot (\nabla \cdot w), \quad (\text{for } w \text{ a vector or tensor field}) \quad (11)$$

$$(R \cdot w)^\top (R \cdot v) = R \cdot (w^\top v), \quad (\text{for } w, v \text{ vector or tensor fields}) \quad (12)$$

Both f and g can be decomposed as linear combinations of

$$(\nabla v)^\top u, \quad \Delta v, \quad \nabla p, \quad \text{and} \quad Te_3, \quad (13)$$

where $v \in \{T, u\}$. Since R 's action is linear, it suffices to show equivariance for these terms individually, i.e.,

$$(\nabla(R \cdot v))^\top (R \cdot u) = R \cdot (\nabla v)^\top u, \quad (14)$$

$$\Delta(R \cdot v) = R \cdot \Delta v, \quad (15)$$

$$\nabla(R \cdot p) = R \cdot \nabla p, \quad \text{and} \quad (16)$$

$$(R \cdot T)e_3 = R \cdot (Te_3). \quad (17)$$

For (14), we apply first (9) and then (12). For (15), note that $\Delta v = \nabla \cdot \nabla v$, and one can thus use first (10) and then (11). Equation (16) follows from (10). Finally, we have for (12),

$$(R \cdot T)e_3 = (T \circ R)e_3 = Te_3 \circ R = A^\top Te_3 \circ R = R \cdot (Te_3), \quad (18)$$

since A leaves e_3 invariant. Therefore, we have

$$f(R \cdot u, R \cdot T, R \cdot p) = R \cdot f(u, T, p) \quad \text{and} \quad g(R \cdot u, R \cdot T, R \cdot p) = R \cdot g(u, T, p).$$

Equation (8) then follows. \square

A.2 Implementation details

The implementation of 3D convolutions with height-dependent kernels and local vertical parameter sharing, as introduced in Section 4.1.2, can be efficiently realized by wrapping 2D convolution operations, avoiding the need for custom CUDA kernels and ensuring compatibility with existing deep learning frameworks like PyTorch or TensorFlow.

We consider feature maps $f : \mathbb{R}^3 \rightarrow \mathbb{R}^C$ represented as 5D tensors of shape $B \times C \times N_1 \times N_2 \times N_3$, where B is the batch size and $N = N_1 \times N_2 \times N_3$ defines the spatial resolution.

3D convolutions with height-dependent kernels. To apply separate kernels for each of the H_{out} vertical positions in the output feature map, we extract vertical receptive fields of size h from the input tensor. Each field has shape $B \times C_{\text{in}} \times N_1 \times N_2 \times h$. These are sliced per target output height and rearranged by merging the input channels and vertical dimensions, resulting in a tensor of shape $B \times (h \cdot C_{\text{in}}) \times N_1 \times N_2$. We then apply a 2D convolution with $h \cdot C_{\text{in}}$ input channels and C_{out} output channels to compute a single output slice at one height.

To parallelize this across all H_{out} heights, we stack the receptive fields along the channel dimension, producing a tensor of shape $B \times (H_{\text{out}} \cdot h \cdot C_{\text{in}}) \times N_1 \times N_2$, and then apply a grouped 2D convolution, dividing the channels into H_{out} groups, each corresponding to a separate height (not to be confused with group-equivariant convolutions [Cohen and Welling, 2016]). After processing, the output tensor is reshaped back to $B \times C_{\text{out}} \times N'_1 \times N'_2 \times H_{\text{out}}$.

Local vertical parameter sharing. To share kernels across neighboring vertical positions, we define a vertical neighborhood of size k , such that each kernel is applied across heights $\{x_3 - k, \dots, x_3 + k\}$, yielding a total of $n = 2k + 1$ receptive fields, cf. Fig. 3 for a sketch. For each output height, we collect all n local receptive fields and apply the same kernel across them.

To handle boundary effects, we learn an additional set of k kernels both for the top and bottom of the domain, ensuring that each vertical position—regardless of its location—receives the same number of kernel applications.

After convolution, the features from all kernels applied to a vertical position are concatenated along the channel dimension, resulting in $C_{\text{out}} = n \cdot C$ output channels, where C is the number of kernels learned per height. All of this can be parallelized by stacking all vertical neighborhoods along the batch dimension and applying a single grouped 2D convolution as described above.

A.3 Training details and computing resources

Both models were trained using the Adam optimizer [Kingma and Ba, 2017] with an MSE loss, a batch size of 64, a learning rate of 1×10^{-3} , and learning rate decay. Training was stopped after convergence of the validation loss. Dropout, D_4 data augmentation, and batch normalization (which was applied only to the autoencoder) were used. The LSTM was trained using backpropagation through time and scheduled sampling [Bengio et al., 2015] for gradual transition from teacher forcing³ to autoregressive predictions.

Training used a total of 3400 GPU hours on NVIDIA A100 GPUs, with 1200 GPU hours dedicated to the models for final evaluation. Hyperparameters were manually tuned due to the long training times. Training the baseline and equivariant autoencoders took approximately 8.2 and 13.7 hours, respectively, averaged over three runs. Notably, the equivariant autoencoder reached the baseline’s final validation loss after only 1.3 hours. The corresponding LSTM models required 33.9 hours for the baseline and 36.4 hours for the equivariant one. At inference time, the equivariant model has a 22% overhead compared to the baseline.

³Teacher forcing uses the ground truth as the LSTM input during training, instead of its previous output.